

Double Gaussian distribution of barrier heights and self-powered infrared photoresponse of InN/AlN/Si (111) heterostructure

Cite as: J. Appl. Phys. 126, 025301 (2019); doi: 10.1063/1.5100066

Submitted: 15 April 2019 · Accepted: 16 June 2019 ·

Published Online: 9 July 2019



Arun Malla Chowdhury,¹  Rohit Pant,¹  Basanta Roul,^{1,2} Deependra Kumar Singh,¹ K. K. Nanda,^{1,a)} and S. B. Krupanidhi^{1,b)}

AFFILIATIONS

¹Materials Research Centre, Indian Institute of Science, Bangalore 560012, India

²Central Research Laboratory, Bharat Electronics, Bangalore 560013, India

a)nanda@iisc.ac.in

b)sbk@iisc.ac.in

ABSTRACT

InN epilayer has been grown by plasma-assisted molecular beam epitaxy on the AlN/n-Si (111) substrate. The self-powered photodetection has been carried out with an infra-red (IR) laser ($\lambda = 1550$ nm, power density ~ 106.2 mW/cm²), where a photoresponsivity was observed to be $3.36 \mu\text{A/W}$ with response times in milliseconds from the InN/AlN/n-Si (111)-based semiconductor-insulator-semiconductor (SIS) interface. Furthermore, to elucidate the vertical electrical transport properties of the SIS interface, low-temperature electrical behavior has been investigated over a range of 100–400 K. Experimental studies revealed an abnormal increase in the barrier height and a decrease in the ideality factor with increasing temperature, suggesting inhomogeneous barrier heights across the heterojunctions. Such inhomogeneity behaviors have been successfully explained on the basis of thermionic emission theory, assuming the existence of a double Gaussian distribution of barrier heights at the heterostructure interface. Moreover, the SIS device structure exhibits mean barrier heights ($\bar{\phi}_{b0}$) of 1.11 and 0.63 eV, respectively, in two temperature regimes, indicating the presence of defect states and inhomogeneity at the interface, which is supported by the nonlinear behavior of the photocurrent with the power density.

Published under license by AIP Publishing. <https://doi.org/10.1063/1.5100066>

INTRODUCTION

Indium nitride (InN) has emerged as a promising semiconductor for infrared (IR) and near-infrared (NIR) optoelectronics because of its narrow bandgap.^{1–9} InN is enriched with superior transport electron properties (low effective mass, high electron mobility, and high saturation drift velocity), which make it suitable for high-frequency and high-speed electronics.^{7,10–12} Recently, InN-based optoelectronic devices have attracted much interest in the NIR range primarily in 1330 and 1550 nm wavelengths range for fiber optic telecommunications.^{13–16} To realize such applications, it is required to grow InN-based heterostructures with high crystalline quality. It has been suggested in various reports that the structural and electrical properties of InN films can be significantly enhanced by using an AlN buffer layer.^{1,9,17–19} Furthermore, AlN is expected to provide excellent rectifying junction characteristics

owing to the reduction in leakage current. In addition, the presence of a large electronic barrier formed by AlN between InN and n-Si results in effective separation of photogenerated charge carriers.

In the present study, an InN/AlN/n-Si (111)-based semiconductor-insulator-semiconductor (SIS) heterostructure has been fabricated and a self-powered photodetection ($\lambda = 1550$ nm) with a vertical transport configuration (top-bottom) has been reported. The self-powered device showed a good responsivity of $3.36 \mu\text{A/W}$ and response and recovery times of 10 ms and 18 ms, respectively, for the power density of 106.2 mW/cm² of the laser. It was also observed that the photocurrent increases with respect to the power density by a power of 1.36, which might be attributed to the presence of traps at the interfaces. The performance and consistency of a heterostructure device rely on the barrier height (BH) and the sharpness of the interface at the junction, though there is a distribution of BH and interface density.^{20–29} In order to investigate

the nature of the interface of the InN/AlN/n-Si (111) heterostructure, a temperature dependent electrical transport study was carried out in the temperature range of 100–400 K. It was observed that the BH and the ideality factor vary with temperature, and BH is inhomogeneous in nature at the heterointerface. The double Gaussian distribution of barrier heights indicates the presence of defect states and inhomogeneity at the interface, which is supported by the nonlinear behavior of photocurrent with the power density.

EXPERIMENTAL SECTION

However, low dissociation temperature, lack of appropriate substrates in terms of lattice mismatch [$\sim 12\%$ for InN/AlN and $\sim 8\%$ for InN/Si (111)], and disparity in thermal expansion coefficients are the main challenges for the growth of epitaxial InN films. Though lattice mismatch between InN and Si is only 8% compared to other substrates, it has been found that the surface of Si gets unintentionally nitrided during the low temperature growth, and an amorphous SiN_x on the Si surface is formed which adversely affects the quality of the InN film.⁷ The InN epilayer of thickness 116 nm was grown on the 100 nm AlN template [grown on n-Si (111), procured by Dr. Fabrice Semond group, CNRS-CRHEA, France] by using an Omicron nanotechnology plasma-assisted molecular beam epitaxy (PAMBE) system. The resistivity of the n-type silicon substrate is $1\text{--}20\ \Omega\ \text{cm}$ and the corresponding conductivity is $1\text{--}0.05\ \Omega^{-1}\ \text{cm}^{-1}$. Before loading into the MBE chamber, acetone and propan-2-ol were used to degrease the AlN/n-Si (111) template. After that, the template was rinsed with de-ionized water. Prior to the growth of the InN thin film, the substrate was thermally cleaned at 810°C for 30 min to remove the residual hydrocarbons. A two-step process was used to grow epilayers of InN. First, a low temperature InN buffer layer was grown at 410°C for 15 min, and then, the substrate temperature was increased to 470°C for high temperature growth and the growth was carried out for 3 h without any intermediate steps. During the growth process, nitrogen pressure and flow rate were kept at 3×10^{-5} mbar and 0.5 sccm, respectively, with the plasma power was fixed at 350 W. Moreover, the In effusion cell temperature was kept constant at 760°C and corresponding beam equivalent pressure (BEP) was maintained at 1.34×10^{-7} mbar.

The structural characterization of the epilayer was carried out by high resolution X-ray diffraction (HRXRD) using a double-crystal

four-circle diffractometer (Bruker-D8 DISCOVER) to know the crystal quality of the film. Further, the structural quality was confirmed by micro-Raman spectroscopy using a 514 nm line of the Ar^+ ion laser. Carrier concentration of the film was obtained by Hall measurements using a HMS 5000 Hall system from Ecopia. Thickness of the epilayer was investigated by field-emission scanning electron microscopy (FESEM). The aluminum circular contacts of diameter $400\ \mu\text{m}$ and thickness 150 nm were made at the top and bottom of the sample by the thermal evaporation technique using a physical mask. Further, the contacts on the sample were annealed in vacuum for the formation of better contact. The Ohmic nature of the contacts on InN and n-Si (111) was also verified. The current–voltage (I–V) characteristics were measured using a Keithley-2420 source measure unit with the LabVIEW interface in the temperature range of 100–400 K, and the infrared photodetection properties were measured using a CNT's MDL-III 1550 nm laser source.

RESULTS AND DISCUSSION

Figure 1(a) represents the HRXRD 2θ – ω scan of the InN film grown on the AlN/Si (111) substrate. From Fig. 1(a), it can be seen that a strong (0002) InN diffracted peak at $2\theta \sim 31.38^\circ$ is present along with substrate peaks. Also, there is no residual indium present in the sample. The crystalline quality of InN layer was further investigated by calculating the full width half maxima (FWHM) from the (0002) symmetric rocking curve of the InN epilayer. The FWHM value of the InN epilayer was found to be 0.61° as shown in Fig. 1(b) and shows high crystalline quality despite the large lattice mismatch with the underlying AlN layer.

Raman spectroscopy was further used to investigate the crystalline quality and lattice structure of the InN film. The room temperature Raman spectrum of the InN film is shown in Fig. 2. The active modes of the InN can be clearly identified. The wurtzite-InN shows E_2 (high) mode at $489\ \text{cm}^{-1}$, $E_1(\text{TO})$ mode at $477\ \text{cm}^{-1}$, $A_1(\text{TO})$ mode at $446\ \text{cm}^{-1}$, and $A_1(\text{LO})$ mode at $586\ \text{cm}^{-1}$.³⁰ The FWHM value of E_2 (high) mode was found to be $6.1\ \text{cm}^{-1}$. Hence, Raman studies confirm the high crystalline quality, and wurtzite lattice structure of the InN film and is in good agreement with HRXRD data.

FESEM as shown in Fig. 3(a) reveals that the InN film grown on the AlN/Si (111) substrate is quite smooth and planar in

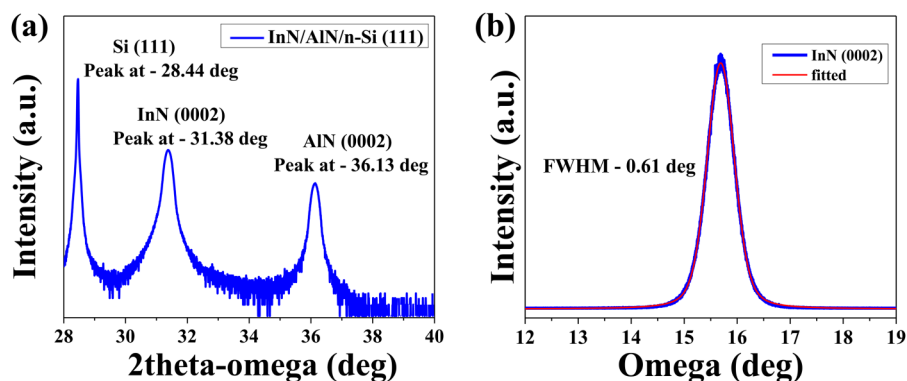


FIG. 1. (a) HRXRD 2θ – ω scans of InN films grown on an AlN template and (b) X-ray rocking curve of the (0002) reflections of the InN epilayer.

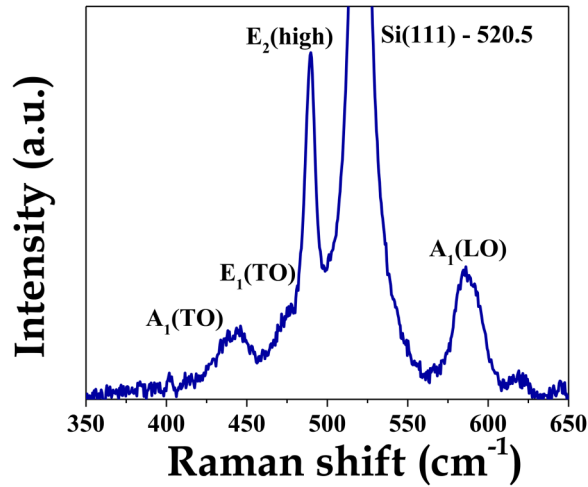


FIG. 2. Room temperature Raman spectrum of the InN epilayer film excited with 514 nm.

nature. Thickness of the film was determined by the cross-sectional FESEM [Fig. 3(b)] and it was found to be 116.6 nm.

Dark I-V characteristics

Room temperature J - V measurements of the device are shown in Fig. 4. The linear nature of Al/InN/Al and Al/Si (111)/Al in Fig. 4 shows that the Al makes a good Ohmic contact with InN and Si layers. The device exhibits excellent rectifying behavior at room temperature similar to other reported SIS interface studies in the literature.^{23,24,31–33} The device shows better rectifying behavior with the AlN buffer layer than the other cases.³⁴

The carrier transport mechanism for the device under zero, forward, and at reverse bias conditions is described using schematics of the band diagram in Fig. 5. The bandgaps of InN, AlN, and n-Si (111) were taken as 0.64 eV, 6.16 eV, and 1.1 eV, respectively.^{34,35} Room temperature Hall measurement was carried out to estimate the carrier concentration of the InN epilayer film, which was found to be $N_d \sim 9.29 \times 10^{19} \text{ cm}^{-3}$ (n^+ -type). The number of states in the conduction band (N_c) for the InN layer is reported to be $0.9 \times 10^{18} \text{ cm}^{-3}$ as per theoretical calculations.³⁶

Now substituting the values of N_c and N_d , the value of $(E_c - E_f)$ at room temperature (300 K) was obtained from the following equation:

$$E_c - E_f = K_B T \ln \left(\frac{N_c}{N_d} \right), \quad (1)$$

where K_B is Boltzmann's constant and T is the temperature.

From Eq. (1), the estimated value of $E_c - E_f$ is -0.12 eV for the InN layer. The value of $(E_c - E_f)$ is a negative quantity, which suggests that the Fermi level (E_f) of the InN layer would lie above the conduction band (E_c) minima of the corresponding layer as shown in Fig. 5(a). To draw the band diagram, the conduction band offset (CBO) and the valence band offset (VBO) for the AlN/n-Si(111) interface were taken to be 1.6 eV and 3.5 eV, respectively.³⁷ Similarly, CBO (ΔE_c) and VBO (ΔE_v) for the InN/AlN interface were taken to be 4.0 eV and 1.52 eV, respectively, from the literature.³⁵

The unintentionally doped InN epilayer reveals n^+ -type conductivity, and the Fermi level lies in the conduction band at the equilibrium condition, as shown in Fig. 5(b). Under forward bias conditions, as shown in Fig. 5(c), electrons dominate the forward bias current. The electrons, which are accumulated near the junction flow across the AlN layer (from InN to Si) when the bias is greater than the threshold voltage. On the other hand, when the junction is reverse biased, the leakage current is very less due to the presence of the insulating AlN layer. Thus, a good rectifying behavior is observed as shown in Fig. 5(d). Holes may dominate the charge transport at high reverse biased.

Photodetection measurements

The photodetection was carried out in the IR region ($\lambda - 1550 \text{ nm}$) because of the bandgap of InN ($E_g - 0.7 \text{ eV}$) as well, which falls in the desired IR region. The current-voltage (I-V) characteristics of the device are represented in Fig. 6, in dark and with light illumination, varying the optical (Laser) power densities between 20.4 and 106.2 mW/cm^2 at a constant wavelength of 1550 nm. An abrupt increase in photocurrent was observed in the region of zero bias compared to any biased conditions, as shown by the inset in Fig. 6. The device displays a maximum photocurrent at a high power density of 106.2 mW/cm^2 . Figure 7(a) shows the temporal photo response and stability of the device at zero bias by switching the laser source (1550 nm) in the off and on states. Figure 7(b) demonstrates the fitted rise and falling curves

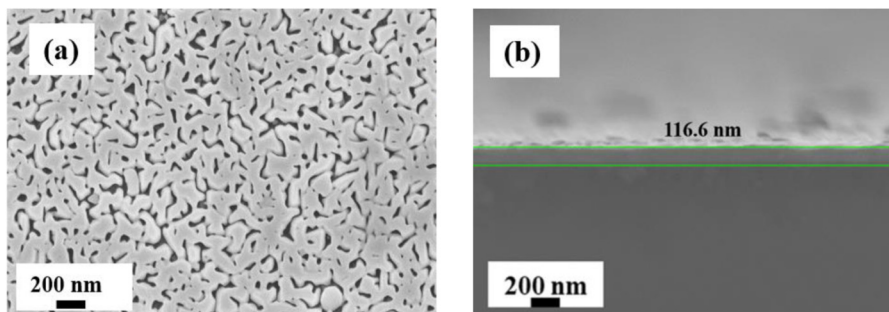


FIG. 3. (a) Top and (b) cross-sectional FESEM images of InN epilayer films.

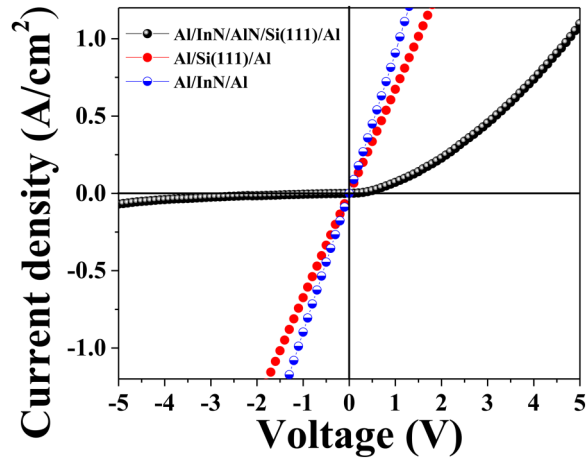
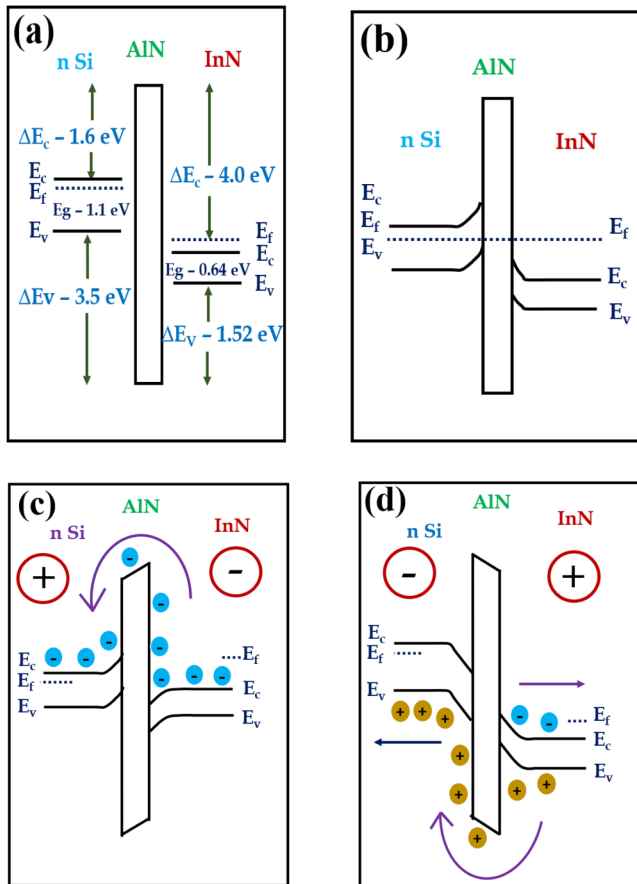
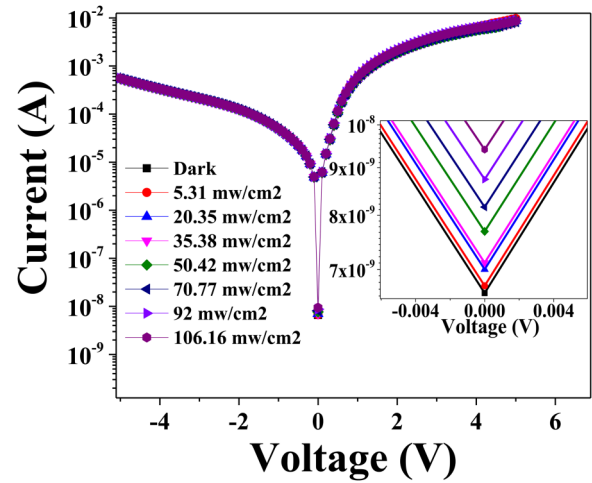
FIG. 4. Room temperature J - V characteristics of various device structures.

FIG. 5. Energy band diagrams of the InN/AlN/n Si(111) S-I-S heterojunction device (a) before equilibrium, (b) after equilibrium (at thermal equilibrium), (c) under the forward bias conditions, and (d) under the reverse bias conditions.

FIG. 6. I - V characteristic of the InN/AlN/n Si (111) detector under dark and light illumination (1550 nm). The inset shows the photocurrent with different power densities at zero bias.

of the self-powered photodetector at an optical power density of 106.2 mW/cm^2 . The response and recovery times were evaluated by using Eqs. (2) and (3), respectively,

$$I(t) = I_{\text{dark}} + A \left\{ 1 - \exp \left(\frac{-(t-t_0)}{\tau_g} \right) \right\}, \quad (2)$$

$$I(t) = I_{\text{dark}} + A \left\{ \exp \left(\frac{-(t-t_0)}{\tau_d} \right) \right\}, \quad (3)$$

where I_{dark} and A are the dark current and scaling constant, respectively. t_0 is the time when light was ON or OFF. τ_g and τ_d are the response time and recovery time constants, respectively. The response and recovery times of the device was found to be 10 ms and 18 ms, respectively, shown in Fig. 7(b).

The performance of a photodetector is determined by responsivity (R_λ), which is defined by $R_\lambda = \frac{I_{ph}}{P_\lambda S}$,⁴⁰⁻⁴² where I_{ph} is the photocurrent, P_λ is the incident power of the light source of wavelength λ , which varies from 20.4 to 106.2 mW/cm^2 , and S is the illuminated junction area of the detector which is 0.785 mm^2 .

The carrier generation mechanism of the InN/AlN/n-Si (111) self-powered photodetector is described through the schematic band diagram as represented in Fig. 7(c). An internal electric field is generated at the InN/AlN interface, which imparts the photoresponse at zero bias. Under the light illumination ($h\nu \geq E_g$), electrons are excited from the valence band to the conduction band in InN. Due to the presence of the internal electric field, the electrons in the conduction band drift and get collected, giving rise to a photocurrent in the device. Therefore, the device exhibits self-powered photodetection.

The dependence of time constants, responsivity, and photocurrent of the device on the power density has been studied at zero bias (Fig. 8). It can be seen that time constants are inversely

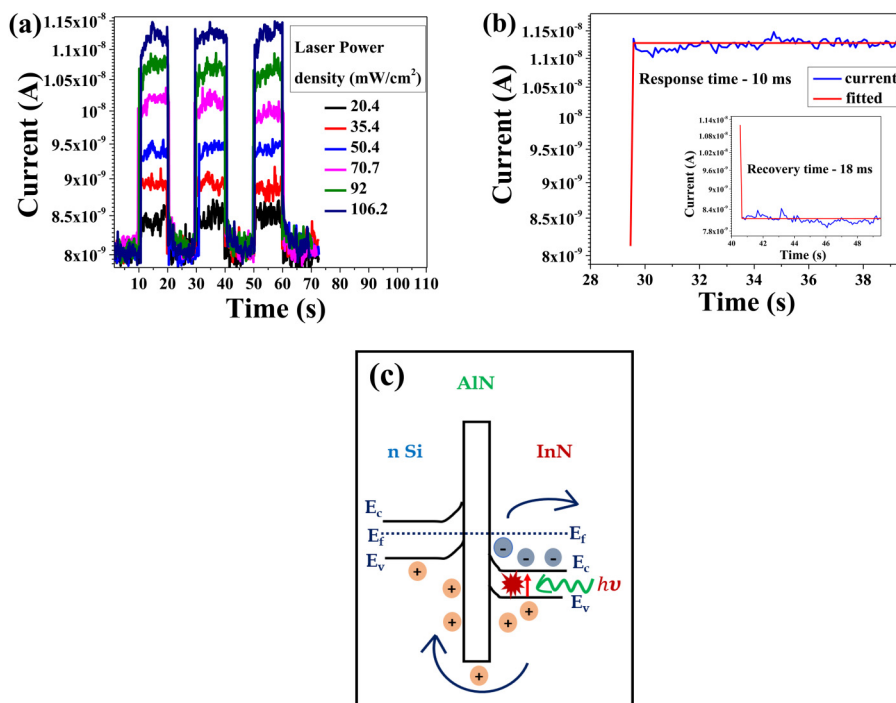


FIG. 7. (a) Temporal response of the photodetector at zero bias with the wavelength of light 1550 nm with different power densities. (b) ON-OFF switching representing the response speed under light illumination at zero bias with a power density of 106.2 mW/cm². (c) Energy band diagram after excitation by 1550 nm of laser light at zero bias.

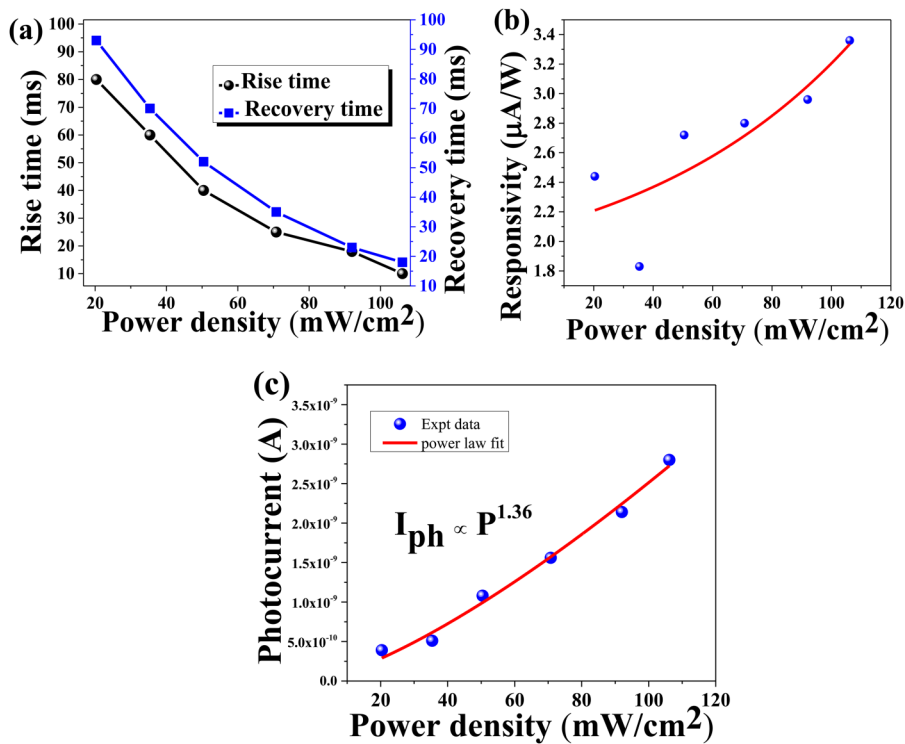


FIG. 8. (a) Dependence of rise time and fall time constants of the InN-based SIS photodetector on the power density at zero bias with 1550 nm wavelength. (b) Responsivity of the InN photodetector in the IR region (1550 nm) with the power density at zero bias. (c) Variation of the photocurrent with the power density at zero bias (1550 nm).

proportional to the power density [Fig. 8(a)]. Therefore, a large number of photons are getting generated due to a high power density, which could lead to faster response times.⁸ The variation of responsivity as a function of the power density is shown in Fig. 8(b) at zero bias. A photoresponsivity of $2.44 \mu\text{A/W}$ was obtained at an illumination power density of 20.4 mW/cm^2 and increases with increasing power density. The device shows relatively lower responsivity, which is obvious for self-powered photodetectors, since there is no external electric field present to separate the electron-hole pairs. The separation of electron-hole pairs in self-powered devices depends on the built-in electric field that helps the detection of light irradiance. The low responsivity could also be attributed due to the presence of barrier height inhomogeneity at the interface. There is a gradual increase in photocurrent with increasing light intensity and it can be seen in Fig. 8(c). The relation between photocurrent and illumination power density can be described by an empirical formula $I_{ph} \propto P_{\lambda}^{\theta}$, where θ is the response between photocurrent and illuminated power density.⁸ The fitted value of θ is found to be 1.36 and the nonunity value of θ illustrates the complex process involved in the photogeneration of carriers through trapping and recombination, etc.^{43–48}

Temperature dependent transport studies

For further investigation of transport mechanisms, the temperature dependent J - V (J - V - T) measurements of the sample were carried out in the temperature range of 100–400 K at an interval of 50 K. Forward J - V characteristics as a function of temperature of the InN/AlN/n-Si (111) device are represented in Fig. 9. It can be seen from the J - V - T curve that the forward current increases with temperature at fixed bias and indicates that the current is induced by the thermionic emission (TE) theory not by the thermionic field emission (TFE) theory because the AlN inter-layer is quite thick to restrict the TFE phenomenon. The linear region of the forward J - V curves is fitted by the TE model, while the BH (ϕ_b) and ideality

factor (η) values were calculated as a function of measuring temperature. Based on the TE theory, the J - V characteristic of an ideal diode at forward bias voltage V , where $V \geq 3KT/q$ and ignoring the BH lowering due to image force, is given by the relation (4),^{49,50}

$$J = J_s \exp\left(\frac{qV}{\eta KT}\right), \quad (4)$$

where

$$J_s = A^* T^2 \exp\left(-\frac{q\phi_b}{KT}\right). \quad (5)$$

Hence, J_s is the reverse of the saturation current density, derived by extrapolating the TE fit at zero bias. Now in relation (5), T is the measurement temperature, A^* is Richardson's constant, K is the Boltzmann's constant, q is the electron charge, ϕ_b is the barrier height, and η is the ideality factor. The theoretical value of A^* for the n-type Si (111) was taken as $112 \text{ A cm}^{-2} \text{ K}^{-2}$ for calculations.⁵¹ The linear region of the J - V characteristics is fitted by Eq. (4) to obtain the values of ϕ_b and η at different temperatures as shown in Fig. 9. Based on the TE model, the derived values of ϕ_b and η are given in Table I. It was observed that ϕ_b has increased and η has decreased with increasing temperature, respectively [Fig. 10(a)]. Temperature dependent ϕ_b and η indicate that the BH is inhomogeneous in nature, and the inhomogeneity could be attributed to dislocation density present at the semiconductor and insulator interfaces.^{9,25,26,52–57} Equation (5) can be reorganized as

$$\ln\left(\frac{J_s}{T^2}\right) = \ln(A^*) - \frac{q\phi_b}{KT}. \quad (6)$$

A plot of $\ln\left(\frac{J_s}{T^2}\right)$ vs $\frac{q}{KT}$, known as Richardson's plot, is shown in Fig. 10(b), which was fitted linearly. The barrier height (ϕ_b) at zero bias was obtained from the linear fit of the slope and Richardson's constant (A^*) has been calculated from the intercept. However, Richardson's plot has two linear temperature ranges. In the first region (250–400 K), values of the barrier height and Richardson's constant are 0.125 eV and $6.81 \times 10^{-7} \text{ A/cm}^2 \text{ K}^2$, respectively, while in the second region (100–200 K), values of the barrier height and Richardson's constant were 0.008 eV and $2.02 \times 10^{-9} \text{ A/cm}^2 \text{ K}^2$, respectively. The derived values of A^* are much lower than the theoretical value of $112 \text{ A/cm}^2 \text{ K}^2$ for the n-type Si. Also, the derived values of barrier height (ϕ_b) are much

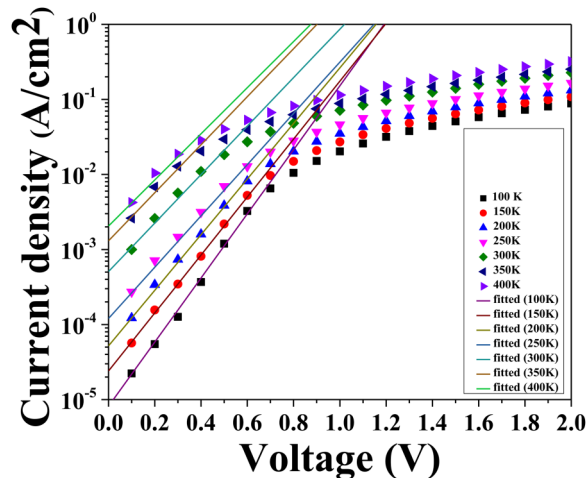


FIG. 9. The forward J - V characteristics as a function of temperature for the device InN/AlN/n-Si (111) and the TE fitting to the J - V characteristics.

TABLE I. Electrical parameters found from J - V measurements at different temperatures.

Temperature (K)	TE	
	η	ϕ_b
100	11.8	0.221
150	8.7	0.328
200	6.8	0.434
250	5.9	0.534
300	5.2	0.613
350	4.5	0.696
400	4.1	0.789

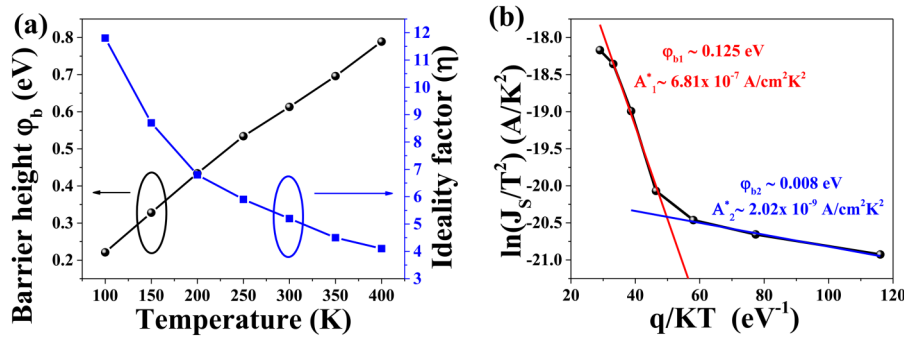


FIG. 10. (a) The temperature dependences of the barrier height and ideality factor derived from the forward J - V data using the TE model. (b) The conventional Richardson's plot of $\ln(J_s/T^2)$ vs q/KT .

lower than the experimental values. The discrepancies in the theoretically and experimentally derived values suggest the formation of inhomogeneous barrier heights at the interfaces.²⁸ The inhomogeneity can be explained by assuming a lateral distribution of the BHs with a Gaussian distribution.^{27,28,58–60} Assuming that the barrier heights follow a Gaussian distribution, therefore, it can be given by the following expression:

$$P(\phi_b) = \frac{1}{\sigma_s \sqrt{2\pi}} \exp \left[-\frac{(\phi_b - \bar{\phi}_b)^2}{2\sigma_s^2} \right], \quad (7)$$

where $\frac{1}{\sigma_s \sqrt{2\pi}}$ stands for the normalization constant, $\bar{\phi}_b$ and σ_s are the mean and the standard deviation of the barrier height, respectively. The total current density at the forward bias then becomes

$$J(V) = \int_{-\infty}^{+\infty} J(\phi_b, V) P(\phi_b) d\phi_b, \quad (8)$$

where $J(\phi_b, V)$ is the current density at the forward bias V for a barrier height ϕ_b . Introducing Eqs. (4) and (7) into Eq. (8) and performing the integration, the resulting equation becomes

$$J(V) = J_s \exp \left(\frac{qV}{\eta_{ap} KT} \right), \quad (9)$$

$$\text{with } J_s = A^* T^2 \exp \left(-\frac{q\phi_{ap}}{KT} \right), \quad (10)$$

where ϕ_{ap} and η_{ap} are the apparent barrier height and apparent

ideality factor, respectively, measured experimentally and given as

$$\phi_{ap} = \bar{\phi}_{b0} - \frac{q\sigma_s^2}{2KT}, \quad (11)$$

$$(\eta_{ap}^{-1} - 1) = \rho_2 - \frac{q\rho_3}{2KT}. \quad (12)$$

Now, $\bar{\phi}_{b0}$ and σ_s are zero bias mean barrier height and standard deviation, respectively, which are linearly bias dependent on Gaussian parameters, such as $\bar{\phi}_b = \bar{\phi}_{b0} + \rho_2 V$ and $\sigma_s = \sigma_{s0} + \rho_3 V$, where ρ_2 and ρ_3 are the voltage coefficients measuring the voltage deformation of the barrier height distribution. A straightline plot of ϕ_{ap} vs $\frac{q}{2KT}$ had offered us the values of $\bar{\phi}_{b0}$ and σ_s , which were derived from the intercept and slope of the straight line [Fig. 11(a)]. Similarly, a linear plot of $(\eta_{ap}^{-1} - 1)$ vs $\frac{q}{2KT}$ had provided us with values of ρ_2 and ρ_3 , which were obtained from the intercept and slope of the straight line [Fig. 11(b)].

The values obtained from linear plots (Fig. 11) quantifying the extent of inhomogeneities exist at the interfaces and also are the evidence of Gaussian distributions of barrier heights. It can be seen from Fig. 11 that there are two linear regions, with transition occurring at 200 K. These results confirm the existence of two Gaussian distributions of barrier heights. Straight lines from Fig. 11(a) provided two sets of values of $\bar{\phi}_{b0}$ and σ_s as 1.11 eV and 0.158 V in the temperature range of 250–400 K (region I) and 0.631 eV and 0.086 V in the temperature range of 100–200 K (region II), respectively. Similarly, from Fig. 11(b), the two sets of

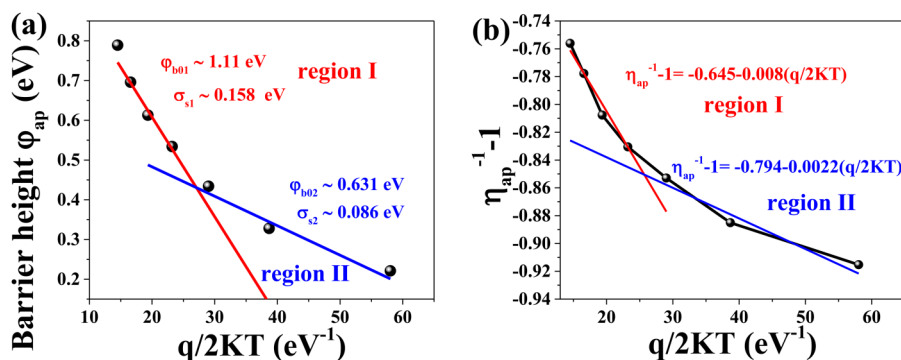


FIG. 11. (a) Apparent barrier height (ϕ_{ap}) vs $q/2KT$ and (b) $(\eta_{ap}^{-1} - 1)$ vs $q/2KT$.

values of ρ_2 and ρ_3 are -0.645 V and 0.008 V in the temperature range of 250 – 400 K (region I) and -0.794 V and 0.0022 V in the temperature range of 100 – 200 K (region II), were obtained, respectively. The slope (ρ_3) of region I is greater than the slope of region II; hence, it can be proposed that region I is wider with relatively higher barrier height. It has been suggested in various reports^{27,58,61–63} that below a certain temperature (junction property), there could be a change in the phase near the junction. This phase change near the junction changes the barrier height, as we were able to observe region II.

Therefore, considering the Gaussian distribution of barrier height inhomogeneity present at the interface, Richardson's equation for two temperature regions can be modified by combining Eq. (5) with Eq. (10) as follows:

$$\ln\left(\frac{J_s}{T^2}\right) - \left(\frac{q^2\sigma_s^2}{2K^2T^2}\right) = \ln(A^*) - \frac{q\bar{\varphi}_{b0}}{KT}. \quad (13)$$

The modified Richardson's plot, i.e., $\ln\left(\frac{J_s}{T^2}\right) - \left(\frac{q^2\sigma_s^2}{2K^2T^2}\right)$ vs $\frac{q}{KT}$, is presented in Fig. 12 for two temperature regions.

The linear fit of the plot in Fig. 12 provides the values of Richardson's constant (A^*) and zero bias mean barrier height ($\bar{\varphi}_{b0}$). Thus, the values of $\bar{\varphi}_{b0}$ and A^* were obtained to be 1.11 eV and 109.94 A/cm² K², respectively, for region I (250 – 400 K), while for region II (100 – 200 K), the values of $\bar{\varphi}_{b0}$ and A^* were derived to be 0.63 eV and 95.58 A/cm² K², respectively. The values of Richardson's constant for both temperature regions derived from the modified Richardson's plot are very close to the theoretical value of 112 A/cm² K² for n-Si. Especially, Richardson's constant value obtained for region I (250 – 400 K) is almost identical to the theoretical value for n-Si. Therefore, the temperature dependence J – V characteristics of InN/AlN/n-Si (111) reveal that the barrier height is not continuous and there exists a double Gaussian distribution of barrier height at the interface over the entire temperature range.

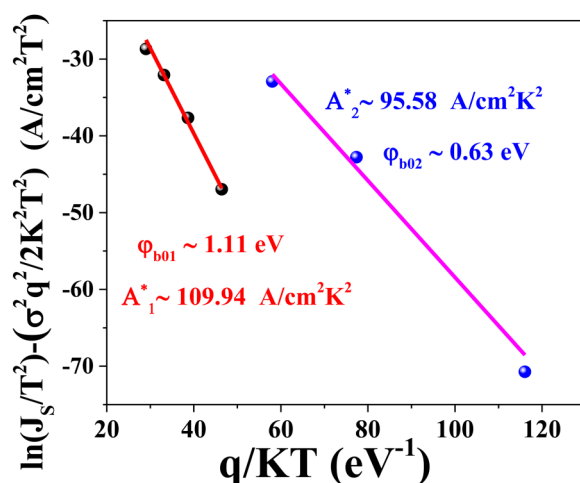


FIG. 12. The modified Richardson's plot.

CONCLUSIONS

The InN epilayer was grown by plasma-assisted molecular beam epitaxy (PAMBE) on the AlN/n-Si (111) substrate. Self-powered photodetection of the device was observed with the IR laser (1550 nm). The self-powered photodetector exhibited a photoresponsivity of 3.36 μ A/W under an illumination power density of 106.2 mW/cm², while offering a faster response time in milliseconds. It was also noticed that the photocurrent increases by a ratio of 1.36 units with respect to the power density, which is attributed due to the presence of traps at the interfaces. Further, to investigate the nature of interface, the forward bias J – V characteristics of the InN/AlN/n-Si (SIS) structure were studied in the temperature range of 100 – 400 K. The temperature dependent barrier height and the ideality factor were observed, i.e., the barrier height increased and the ideality factor decreased with increasing substrate temperature. The temperature dependent barrier height indicates that the BH is inhomogeneous across the heterojunctions and follows a double Gaussian distribution with mean barrier heights ($\bar{\varphi}_{b0}$) of 1.11 and 0.63 eV. This present work is thus believed to open up a new technical route for InN-based SIS heterojunction photodetectors to be used in nanoscale electronics, optoelectronics, integrated circuits, and fiber optic telecommunications, which can be used in fiber optic telecommunications, etc., and also elaborates the necessary interface properties with the help of modified Richardson's equation to study the heterostructure, which enables such types of photodetection properties.

REFERENCES

- G. Gwo, C.-L. Wu, C.-H. Shen, W.-H. Chang, T. M. Hsu, J.-S. Wang, and J.-T. Hsu, *Appl. Phys. Lett.* **84**, 3765 (2004).
- B. Monemar, P. P. Paskov, and A. Kasic, *Superlattices Microstruct.* **38**, 38 (2005).
- V. Y. Davydov, A. A. Klochikhin, R. P. Seisyan, V. V. Emtsev, S. V. Ivanov, F. Bechstedt, J. Furthmüller, H. Harima, A. V. Mudryi, J. Aderhold, O. Semchinova, and J. Graul, *Physica Status Solidi B* **229**, R1–R3 (2002).
- J. Wu, W. Walukiewicz, K. M. Yu, J. W. Ager, E. E. Haller, H. Lu, W. J. Schaff, Y. Saito, and Y. Nanishi, *Appl. Phys. Lett.* **80**, 3967 (2002).
- T. Matsuoka, H. Okamoto, M. Nakao, H. Harima, and E. Kurimoto, *Appl. Phys. Lett.* **81**, 1246 (2002).
- K. Xu and A. Yoshikawa, *Appl. Phys. Lett.* **83**, 251 (2003).
- A. G. Bhuiyan, A. Hashimoto, and A. Yamamoto, *J. Appl. Phys.* **94**, 2779 (2003).
- S. Krishna, A. Sharma, N. Aggarwal, S. Husale, and G. Gupta, *Sol. Energy Mater. Sol. Cells* **172**, 376 (2017).
- C. L. Wu, C. H. Shen, H. W. Lin, H. M. Lee, and S. Gwo, *Appl. Phys. Lett.* **87**, 241916 (2005).
- B. E. Foutz, S. K. O'Leary, M. S. Shur, and L. F. Eastman, *J. Appl. Phys.* **85**, 7727 (1999).
- I. Vurgaftman, J. R. Meyer, and L. R. Ram-Mohan, *J. Appl. Phys.* **89**, 5815 (2001).
- S. K. O'Leary, B. E. Foutz, M. S. Shur, U. V. Bhapkar, and L. F. Eastman, *J. Appl. Phys.* **83**, 826 (1998).
- M. H. Polash, *Opt. Eng.* **57**, 0–7 (2018).
- Md. Mobarak Hossain Polash, and M. Shah Alam, *ECS Transactions* **69**, 71 (2015).
- K. Schires, R. Al Seyab, A. Hurtado, V. Korpiljärvi, I. D. Henning, M. J. Adams, C. Orc, P. O. Box, and F. Tampere, *Opt. Express* **20**, 3550 (2012).
- S. R. Bank, B. Hopil, L. L. Goddard, H. B. Yuen, M. A. Wistey, R. Kudrawiec, and J. S. Harris, *IEEE J. Quantum Electron.* **43**, 773 (2007).

- ¹⁷C.-L. Wu, C.-H. Shen, H.-Y. Chen, S.-J. Tsai, H.-W. Lin, H.-M. Lee, S. Gwo, T.-F. Chuang, H.-S. Chang, and T. M. Hsu, *J. Cryst. Growth* **288**, 247 (2006).
- ¹⁸T. Yamaguchi, Y. Saito, C. Morioka, K. Yorozu, T. Araki, A. Suzuki, and Y. Nanishi, *Phys. Status Solidi B* **240**, 429 (2003).
- ¹⁹H. Lu, W. J. Schaff, J. Hwang, H. Wu, G. Koley, and L. F. Eastman, *Appl. Phys. Lett.* **79**, 1489 (2001).
- ²⁰A. Singh, *Solid State Electron.* **28**, 223 (1985).
- ²¹H. C. Card and E. H. Rhoderick, *J. Phys. D: Appl. Phys.* **4**, 1589 (1971).
- ²²P. Chattopadhyay and B. RayChaudhuri, *Solid State Electron.* **36**, 605 (1993).
- ²³H. Jeong, S. Bang, H. M. Oh, H. J. Jeong, S.-J. An, G. H. Han, H. Kim, K. K. Kim, J. C. Park, Y. H. Lee, G. Lerondel, and M. S. Jeong, *ACS Nano* **9**, 10032 (2015).
- ²⁴J. Shewchun, J. Dubow, C. W. Wilmsen, R. Singh, D. Burk, and J. F. Wager, *J. Appl. Phys.* **50**, 2832 (1979).
- ²⁵Ş. Karataş, Ş. Altındal, A. Tüürüt, and A. Özmen, *Appl. Surf. Sci.* **217**, 250 (2003).
- ²⁶F. E. Cimilli, M. Salam, and A. Tüürüt, *Semicond. Sci. Technol.* **22**, 851 (2007).
- ²⁷A. F. Özdemir, A. Turut, and A. Kökçe, *Semicond. Sci. Technol.* **21**, 298 (2006).
- ²⁸R. T. Tung, *Mater. Sci. Eng. R Rep.* **35**, 1 (2001).
- ²⁹S. M. Sze and K. K. Ng, *Physics of Semiconductor Devices* (Wiley-Interscience, 2007).
- ³⁰M. Kumar, M. K. Rajpalke, T. N. Bhat, B. Roul, N. Sinha, A. T. Kalghatgi, and S. B. Krupanidhi, *Mater. Lett.* **65**, 1396 (2011).
- ³¹J. Shewchun, J. Dubow, A. Myszkowski, and R. Singh, *J. Appl. Phys.* **49**, 855 (1978).
- ³²W. Wang, C. Chen, G. Zhang, T. Wang, H. Wu, Y. Liu, and C. Liu, *Nanoscale Res. Lett.* **10**, 91 (2015).
- ³³H. Zhu, C. X. Shan, L. K. Wang, J. Zheng, J. Y. Zhang, B. Yao, and D. Z. Shen, *J. Phys. Chem. C* **114**, 7169 (2010).
- ³⁴M. Kumar, B. Roul, T. N. Bhat, M. K. Rajpalke, A. T. Kalghatgi, and S. B. Krupanidhi, *Phys. Status Solidi Appl. Mater. Sci.* **209**, 994 (2012).
- ³⁵P. D. C. King, T. D. Veal, P. H. Jefferson, C. F. McConville, T. Wang, P. J. Parbrook, H. Lu, and W. J. Schaff, *Appl. Phys. Lett.* **90**, 132105 (2007).
- ³⁶P. Mahala, S. K. Behura, A. Ray, C. Dhanavantri, and O. Jani, *Opt. Quantum Electron.* **47**, 1117 (2015).
- ³⁷S. W. King, R. J. Nemanich, and R. F. Davis, *J. Appl. Phys.* **118**, 045304 (2015).
- ³⁸B. Roul, R. Pant, A. M. Chowdhury, G. Chandan, D. K. Singh, S. Chirakkara, K. K. Nanda, and S. B. Krupanidhi, *IEEE Trans. Electron. Devices* **66**, 1345 (2019).
- ³⁹R. Pant, A. Shetty, G. Chandan, B. Roul, K. K. Nanda, and S. B. Krupanidhi, *ACS Appl. Mater. Interfaces* **10**, 16918 (2018).
- ⁴⁰S. Manna, S. Das, S. P. Mondal, R. Singha, and S. K. Ray, *J. Phys. Chem. C* **116**, 7126 (2012).
- ⁴¹T. Yang, K. Sun, X. Liu, W. Wei, T. Yu, X. Gong, D. Wang, and Y. Cao, *J. Phys. Chem. C* **116**, 13650 (2012).
- ⁴²J. Ding, S. Du, Z. Zuo, Y. Zhao, H. Cui, and X. Zhan, *J. Phys. Chem. C* **121**, 4917 (2017).
- ⁴³A. Rose, *Concepts in Photoconductivity and Allied Problems* (Krieger, New York, 1978).
- ⁴⁴S. Choi and S. A. Rice, *J. Chem. Phys.* **38**, 366 (1963).
- ⁴⁵N. Almeleh and S. E. Harrison, *J. Phys. Chem. Solids* **26**, 1571 (1965).
- ⁴⁶R. C. J. Silver, M. D. Olness, and M. Swicord, *Phys. Rev. Lett.* **10**, 12 (1963).
- ⁴⁷J. Zou, Q. Zhang, K. Huang, and N. Marzari, *J. Phys. Chem. C* **114**, 10725 (2010).
- ⁴⁸A. M. Chowdhury, G. Chandan, R. Pant, B. Roul, D. K. Singh, K. K. Nanda, and S. B. Krupanidhi, *ACS Appl. Mater. Interfaces* **11**, 10418 (2019).
- ⁴⁹H. Morkoç and H. Morkoç, *Handbook of Nitride Semiconductors and Devices* (Wiley-VCH, 2008).
- ⁵⁰M. Shur, *Physics of Semiconductor Devices* (Prentice-Hall, Engelwood Cliffs, NJ, 1990).
- ⁵¹M. Kumar, B. Roul, M. K. Rajpalke, T. N. Bhat, A. T. Kalghatgi, and S. B. Krupanidhi, *Curr. Appl. Phys.* **13**, 26 (2013).
- ⁵²V. Kumar, S. C. Jain, A. K. Kapoor, J. Poortmans, and R. Mertens, *J. Appl. Phys.* **94**, 1283 (2003).
- ⁵³F. E. Jones, B. P. Wood, J. A. Myers, C. Daniels-Hafer, and M. C. Lonergan, *J. Appl. Phys.* **86**, 6431 (1999).
- ⁵⁴B. Roul, T. N. Bhat, M. Kumar, M. K. Rajpalke, N. Sinha, A. T. Kalghatgi, and S. B. Krupanidhi, *Solid State Commun.* **151**, 1420 (2011).
- ⁵⁵B. Roul, M. K. Rajpalke, T. N. Bhat, M. Kumar, N. Sinha, A. T. Kalghatgi, and S. B. Krupanidhi, *J. Appl. Phys.* **109**, 3 (2011).
- ⁵⁶A. Hattab, J. L. Perrossier, F. Meyer, M. Barthula, H. J. Osten, and J. Griesche, *Mater. Sci. Eng. B Solid State Mater. Adv. Technol.* **89**, 284 (2002).
- ⁵⁷Ş. Altındal, I. Dökme, M. M. Bülbül, N. Yalçın, and T. Serin, *Microelectron. Eng.* **83**, 499 (2006).
- ⁵⁸O. Pakma, N. Serin, T. Serin, and Ş. Altındal, *J. Appl. Phys.* **104**, 014501 (2008).
- ⁵⁹J. H. Werner and H. H. Güttler, *J. Appl. Phys.* **69**, 1522 (1991).
- ⁶⁰S. Acar, S. Karadeniz, N. Tuğluoğlu, A. B. Selçuk, and M. Kasap, *Appl. Surf. Sci.* **233**, 373 (2004).
- ⁶¹Z. Shi-Yang, R. Guo-Ping, Q. Xin-Ping, L. Bing-Zong, R. L. Van Meirhaeghe, C. Detavernier, and F. Cardon, *Chin. Phys.* **11**, 156 (2002).
- ⁶²Ş. Huang and F. Lu, *Appl. Surf. Sci.* **252**, 4027 (2006).
- ⁶³Ö. Güllü, M. Biber, S. Duman, and A. Tüürüt, *Appl. Surf. Sci.* **253**, 7246 (2007).